# Dissociative Photoionization of Quinoline and Isoquinoline

Jordy Bouwman,*,[†] Bálint Sztáray,[‡] Jos Oomens,[†,§] Patrick Hemberger,[‖] and Andras Bodi[‖]

[†]Institute for Molecules and Materials, FELIX Laboratory, Radboud University Nijmegen, Toernooiveld 7c, NL-6525 ED Nijmegen, The Netherlands

[‡]Department of Chemistry, University of the Pacific, Stockton, California 95211, United States

[§]van't Hoff Institute for Molecular Sciences, University of Amsterdam, Science Park 904, NL-1098 XH Amsterdam, The Netherlands

[‖]Molecular Dynamics Group, Paul Scherrer Institut, 5232 Villigen, Switzerland

ABSTRACT: Two nitrogen-containing polycyclic aromatic hydrocarbon isomers of C_9H_7N composition, quinoline, and isoquinoline have been studied by imaging photoelectron photoion coincidence spectroscopy at the VUV beamline of the Swiss Light Source. High resolution threshold photoelectron spectra have been recorded and are interpreted applying a Franck–Condon model. Dissociative ionization mass spectra as a function of the parent ion internal energy are analyzed with the use of breakdown diagrams. HCN loss and H loss are the dominant dissociation paths for both $C_9H_7N^{\bullet+}$ isomers at photon energies below 15.5 eV. Computed $C_9H_7N^{\bullet+}$ potential energy surfaces suggest that the lowest energy path leading to HCN-loss yields the benzocyclobutadiene cation. A statistical model is used to fit the breakdown diagram and—to account for the kinetic shift—the time-of-flight mass spectra that reveal the dissociation rates. We have derived appearance energies of 11.9 ± 0.1 (HCN loss) and 12.0 ± 0.1 (H loss), as well as 11.6 ± 0.2 (HCN loss) and 12.1 ± 0.2 (H loss) eV, for the dissociative ionization of quinoline and isoquinoline, respectively. The results are compared to a recent study on the dissociative ionization of naphthalene. Implications for the formation and destruction of nitrogenated PAHs in the interstellar medium and in Titan's atmosphere are highlighted.
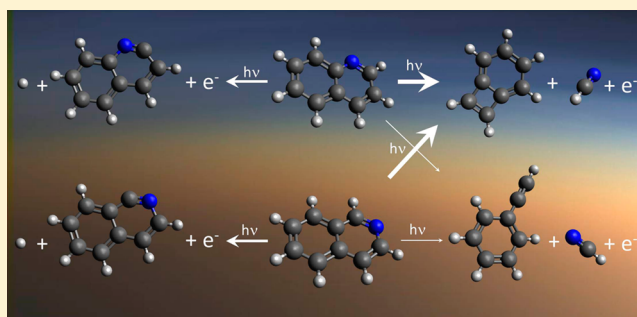
1. INTRODUCTION

Neutral and ionic polycyclic aromatic hydrocarbons (PAHs) and their nitrogenated analogs (azaarenes, PANHs) are found in a large variety of environments, such as planetary atmospheres and the interstellar medium. They have been detected in flames and are precursors to larger molecules that eventually lead to the formation of soot.[1] PANHs are emitted on a large scale as a side product of fossil fuel combustion and are present in the biosphere.[2,3] They exhibit enhanced toxicity and solubility in water compared with their PAH counterparts.[4]

PAHs are postulated to be carriers of the mid-infrared (mid-IR) emission bands that are observed toward numerous objects in the interstellar medium.[5−8] They are believed to be formed in the outflow of carbon rich stars.[9,10] After excitation by (vacuum) ultraviolet (UV) photons, PAHs emit infrared radiation at frequencies typical for aromatic CC and CH vibrational modes. However, the slight variations in the position of the ubiquitous emission band at 6.2 μm cannot be explained by pure PAH emission and it has been suggested that this band arises from inclusion of nitrogen atoms in the PAH molecule.[11,12] Small interstellar PA(N)Hs dissociate in the strong interstellar radiation field, feeding back neutral and charged fragments, and only large PA(N)Hs survive in the interstellar medium.[8,13]

Recently, high molecular weight positive and negative ions were discovered in Titan's atmosphere.[14,15] The positive ions were attributed to fused-ring polycyclic aromatic hydrocarbon compounds such as naphthalene and anthracene.[15] It is widely believed that these molecules are the precursors to particles that compose the yellow haze that shrouds this moon.[16,17] Observations, models, and laboratory experiments have shown that the ion−neutral chemistry leads to complex nitrogen-containing organics.[18−20] Nitrogen-containing PAHs have been identified in laboratory experiments,[21] and it is suggested that they are formed in Titan's upper atmosphere,[22,23] where they may have a significant influence on the temperature and chemistry, because they are strong (V)UV absorbers.

The smallest PAH, naphthalene ($C_{10}H_8$), has recently been investigated,[24] employing tandem mass spectrometry and imaging photoelectron photoion coincidence (iPEPICO) mass spectrometry. It was found that the main dissociative ionization paths below 18 eV are C_2H_2 loss and H loss from the parent ion to form $C_8H_6^{\bullet+}$ and $C_{10}H_7^+$, respectively. In addition, iPEPICO measurements often yield insights into the

dissociation mechanism,[25] the impact parameter of the reverse reaction based on the observed kinetic energy release distributions,[26] or can be used to obtain accurate barriers for the reverse, association reaction.[27] Therefore, they can also be of use to better understand PAH formation reactions.

Here, we present a study of the dissociative photoionization of the smallest PANH isomers quinoline (Q) and isoquinoline (IQ). High-resolution threshold photoelectron spectra are measured and the parent and fragment ion abundances that result from photodissociation are recorded as a function of the internal energy of the parent ion. The potential energy surface that leads to the detected fragments is mapped through quantum chemical computations. Rice−Ramsperger−Kassel−Marcus (RRKM) simulations are subsequently employed to model the dissociation kinetics.

2. EXPERIMENTAL SECTION

The experiments have been performed on the iPEPICO instrument at the X04DB Vacuum Ultraviolet (VUV) beamline of the Swiss Light Source. A detailed description of the beamline and of the iPEPICO instrument can be found elsewhere,[28,29] and the apparatus will only be described briefly here.

Quinoline and isoquinoline (C_9H_7N, ≥98% and ≥97%, respectively, Scheme 1) were purchased from Sigma−Aldrich

Scheme 1. Structures of the C_9H_7N Isomers Quinoline (Left) and Isoquinoline (Right)
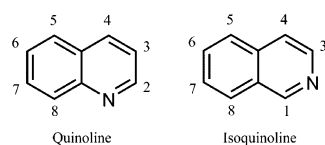
and used without further purification. The sample was introduced into the ionization chamber through a 6 mm outer diameter Teflon tube at room temperature. Here, the effusive sample beam was intersected with the monochromatic radiation of the VUV beamline. The photon energy was

scanned between 8 and 15 eV with step sizes ranging from ∼0.01 to 0.1 eV.

Photoelectrons and -ions are extracted using a continuous 120 V cm^{-1} electric field. Electrons are velocity map imaged onto a delay-line RoentDek imaging detector, and their arrival time also provides the start signal for the coincident photoions' time-of-flight (TOF) analysis. The photoions are space focused on a nonimaging MCP detector and mass analyzed. Owing to the low extraction field and long extraction region, cations have a long residence time in the first acceleration region. If a dissociation is not prompt, but takes place in this region, typically within a few microseconds, the resulting broad and asymmetric daughter ion TOF peak shapes reflect the dissociation rate constant. This way, dissociation rates can be measured in the 10^3-10^7 s^{-1} range and the modeled rates are then fitted to the experimental data using the ion optics parameters.[30] Thus, the kinetic shift is taken into account in the model and accurate dissociation barrier heights are derived.

Threshold electrons are imaged onto a small area in the center of the imaging detector with a kinetic energy resolution better than 1 meV. Energetic ("hot") electrons with zero lateral velocity component are also imaged in the center spot on the detector, and their contribution needs to be subtracted from the threshold electron signal in the center. A small ring area around the center spot[31,32] is defined to correct for hot electron contributions and to obtain threshold electron counts and TPEPICO mass spectra. The former can be used to plot threshold photoelectron spectra (TPES). From the latter, the fragment and parent ion peaks are integrated and their fractional abundances are plotted in the breakdown diagram.

3. COMPUTATIONAL METHODS

DFT calculations were performed using the Gaussian09 suite of programs.[33] The vibrational frequencies and rotational constants of the neutral are used to calculate the internal energy distribution, which is assumed to be shifted to the ion manifold by the photon energy minus the ionization energy. The density of states of the dissociating ion as well as the number of states (sum of states) of the transition state are needed to calculate dissociation rate constants. Potential energy
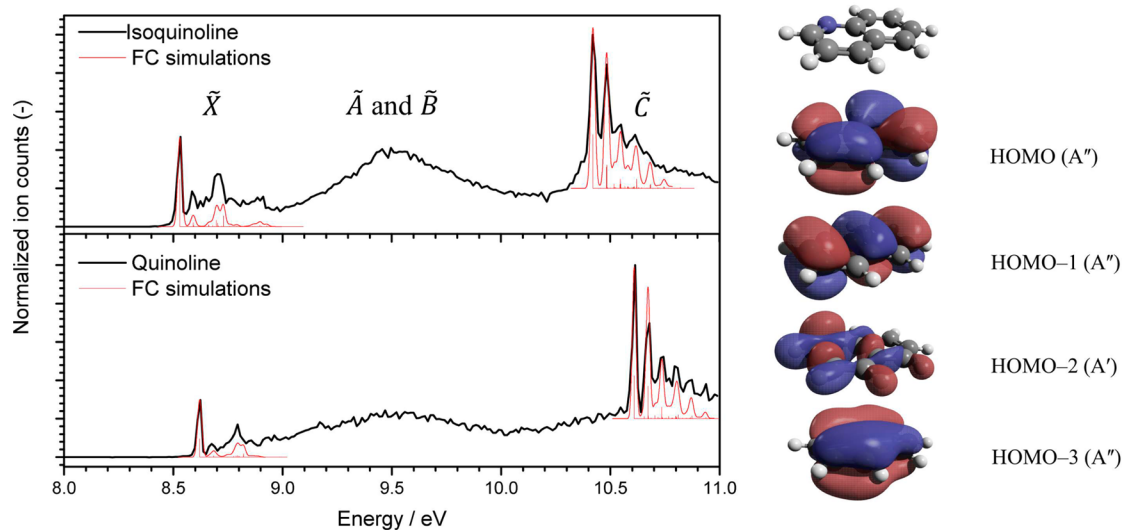
Figure 1. Threshold photoelectron spectra (in black) of quinoline (bottom) and isoquinoline (top) displayed together with Franck−Condon simulated spectra (red). The molecular orbitals of interest are shown on the right-hand side below the quinoline structure.
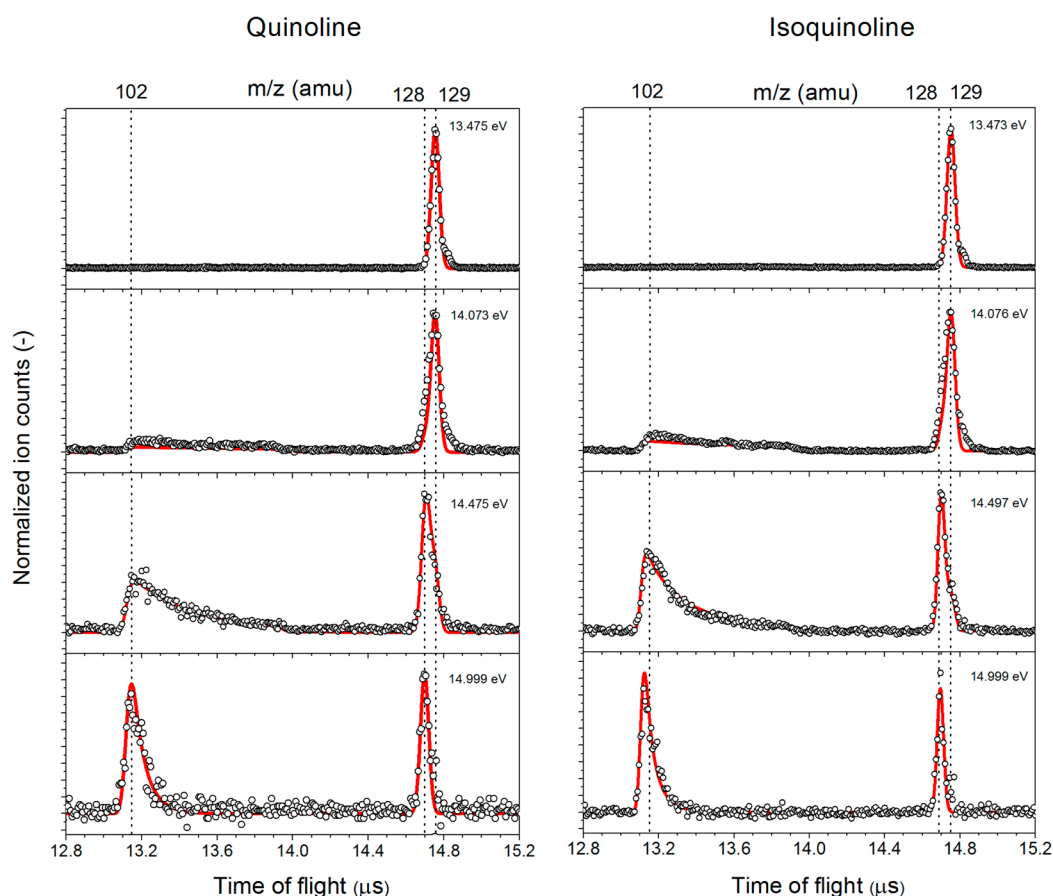
Figure 2. Normalized threshold photoelectron−photoion coincidence mass spectra of quinoline (left) and isoquinoline (right) for a set of four energies (open circles), plotted together with model fits to the data (solid red lines). The dotted lines mark the positions of the parent and daughter ion peaks and their respective *m/z* values.

surface (PES) scans at the B3LYP/6-311++G(d,p) level of theory were carried out to locate (rate-determining) transition states and intermediates that lead to the formation of the detected dissociation products. In the PES scans, the C···C or C···N distance in the C_5N ring system was decreased to yield intermediates, or C−C and C−N bond lengths were increased to explore the bond rupture coordinate. Subsequently, the energetics of the neutral species, cations, intermediates, and transition states located in PES scans were calculated using the CBS-QB3 composite method.[34,35]

Quinoline and isoquinoline are shown to undergo parallel H and HCN loss in the studied energy range. The rate curves for these processes, $k(E)$, determine the relative rates, which in turn define the branching ratios. Because of the relatively tight transition states combined with the large density of states of the dissociating ion, the dissociation rate at threshold is less than the 10^3 s^{-1} needed to observe the fragment ion in the iPEPICO setup. The excess energy required for the parent ion to dissociate on the time scale of the experiment is the kinetic shift. The PEPICO modeling program by Sztáray et al.[30] is employed to calculate the branching ratios in the breakdown diagram and to fit the measured time-of-flight peaks to extract dissociation rates. Computed vibrational modes and rotational constants of the transition states involved in the dissociation serve as input for the program as well as additional experimental parameters, such as sample temperature and ion optics configuration. We have used rigid activated complex (RAC) RRKM theory to calculate the rate curves and fitted the

barrier heights and the transitional frequencies of the transition state model to reproduce the experimental data. Franck−Condon analyses were performed on the basis of optimized DFT and TD-DFT (time-dependent DFT for excited electronic states) geometries and Hessian matrices, applying the program eZspectrum.[36]

4. RESULTS

4.1. Threshold Photoelectron Spectra. High-resolution threshold photoionization spectra were recorded for quinoline and isoquinoline and are displayed in Figure 1. To suppress the effect of volatile contaminants, mostly water and a small, unidentified contaminant at *m/z* = 91, the spectra were recorded by measuring threshold photoelectrons in coincidence with the (iso)quinoline parent ion. The 0−0 transition into the ground electronic state of the cation is very intense in both samples, indicating small geometry change upon ionization. The adiabatic ionization energy can thus be determined as the maximum of this peak with the error bars corresponding to its half width at half-maximum. The ionization threshold is determined to be (8.61 ± 0.02) eV and (8.53 ± 0.02) eV for quinoline and isoquinoline, respectively. These values compare well with 8.62 and 8.54 eV for quinoline and isoquinoline, respectively, recorded on a commercial photoelectron spectrometer.[37−39] Franck−Condon simulations (Figure 1) for the $\tilde{X}^+$ states reproduce the band positions between 8.5 and 9 eV very well, which are mostly due to excitations into totally symmetric ring deformation modes of the ion ground state.

Roughly 60 meV to the blue of the origin, a bending vibration associated with the nitrogen atom is excited (520 cm^{-1} for quinoline and 490 cm^{-1} for isoquinoline). Between 8.7 and 8.8 eV several unresolved transitions contribute to a broad band in the TPES.

The photoelectron spectra in Figure 1 can be compared with previously published measurements. Brogli et al.[38] reported photoelectron spectra of both isomers and assigned the observed bands. The spectral resolution of the threshold electron spectra presented here allows resolving the structure in the electronic bands at energies below 11 eV. The spectra can also be compared with that of naphthalene, as also reported by Brogli et al.[38] and more recently by Mayer et al.[40] The high-lying occupied molecular orbitals of quinoline are shown in Figure 1. The electronic structure of quinoline and the isoelectronic naphthalene is quite similar. However, the MO analogous to the HOMO−4 σ-type C−H bonding orbital of A′ symmetry in naphthalene also assumes N-lone pair character in quinoline and is thus destabilized and corresponds to HOMO−2. Consequently, there is one more electronic state below the vibrationally well-resolved $\tilde{C}^+$ $^2A''$ state at about 10.5 eV (10 eV in naphthalene). The naphthalene cation electronic states are predicted well by the outer valence Green's function (OVGF) calculations of Mayer et al. as well as TD-DFT calculations.[40] In contrast, the $\tilde{A}^+$ and $\tilde{B}^+$ states of the quinoline cation do not show distinguished features in the TPE spectrum. The fact that the broad band around 9.5 eV is obtained both in the conventional photoelectron spectroscopy measurement of Brogli et al.[38] and in our TPES shows that it is not a result of autoionization processes. Instead, true ion states with reasonable Franck−Condon overlap are expected in this energy range. TD-DFT calculations at the B3LYP/6-311++G(d,p) level, however, suggest that the vertical ionization energy to these states should only be 0.48 and 0.59 eV above the ground electronic cationic state for $\tilde{A}^+$ $^2A''$ and $\tilde{B}^+$ $^2A'$ in quinoline, i.e., at 9.09 and 9.20 eV. EOM-IP-CCSD calculations, carried out using the cc-pVTZ basis set with QChem 4.0.1,[41] are somewhat easier to reconcile with the experimental spectrum and predict vertical ionization energies of 8.64, 9.01, 9.43, and 10.80 eV for the $\tilde{X}^+$ $^2A''$, $\tilde{A}^+$ $^2A''$, $\tilde{B}^+$ $^2A'$, and $\tilde{C}^+$ $^2A''$ states, respectively. The TPES shows a maximum at 9.5 eV, ca. 0.9 eV above the ground state peak, and there is no indication of two electronic states in this band, possibly because of vibronic coupling with another state and the resulting short lifetimes. The $\tilde{C}^+$ $^2A''$ band sets in at 10.4 and 10.6 eV in isoquinoline and quinoline, respectively, and shows vibrational fine structure. This indicates a relatively small geometry change as well as a long enough lifetime of the electronically excited state. The spacing of the vibrational states, at ca. 500 cm^{-1} in both cases, hints at totally symmetric modes, which correspond to stretching the molecule along the axis in the molecular plane that crosses both ring units. Indeed, TD-DFT calculations for the $\tilde{C}^+$ states confirm the distortion of the geometry along these normal modes upon ionization. According to the Franck−Condon simulation, the C−C−C bending motion (508 cm^{-1}) is the main carrier of the progression in quinoline. In isoquinoline, a C−C−C (514 cm^{-1}) and a C−C−N (498 cm^{-1}) bending vibration are excited and contribute to the spectrum.

4.2. Breakdown Diagrams. Threshold photoelectron photoion coincidence mass spectra were recorded with a step size of 50 meV in the photon energy range relevant for the lowest energy dissociative photoionization processes, namely from 13.5 to 15.5 eV. Four selected threshold ionization mass spectra for the dissociative ionization of quinoline and isoquinoline for photon energies ranging from 13.475 to 14.999 eV and with the characteristic daughter ion peak shapes indicating a metastable parent ion are displayed in Figure 2.

Dissociative ionization with photon energies up to 15 eV yields main products at m/z = 102 and 128, and the corresponding dissociation channels are shown in Scheme 2.

Scheme 2. Possible Products Formed from the Dissociative Photoionization of Quinoline and Isoquinoline[a]
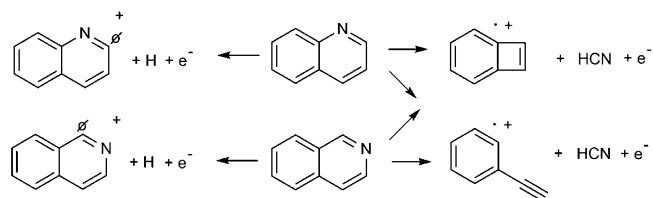
[a]The ø symbol marks the position where the H is likely lost.

Dissociative ionization of the parent ion leading to $C_8H_6^{\bullet+}$ is a slow process, as evidenced by the asymmetric peak shape at m/z = 102 (Figure 2, starting at 13.15 μs). As can be seen from Figure 2, the rate of dissociation increases as the internal energy of the molecule increases, ultimately yielding a nearly symmetric peak profile at high internal energies. The remaining asymmetry in the daughter ion peak at large internal energies (>15.5 eV) is caused by a contribution of C_2H_2 loss that starts to compete and shows up at m/z = 103. For both quinoline and isoquinoline, the C_2H_2-loss contribution comprises 20% of the total m/z =102 and 103 band at internal energies of the parent cation exceeding 15.5 eV. The contribution of C_2H_2 loss to the measured signal drops toward lower internal energies of the parent ion, as is discussed in more detail in the computational section.

Breakdown diagrams are constructed by plotting the fractional abundances of the parent and daughter ion peaks as a function of photon energy. The HCN-loss channel at m/z = 102 is integrated over the full width of the peak. Because of the low extraction field and the resulting instrumental peak width at room temperature, the mass resolution of the apparatus is insufficient to resolve the parent ion and the neighboring hydrogen-loss channel daughter ion. As was first applied to plot the breakdown diagram of naphthalene,[24] the center of gravity of the parent and H-loss band is determined according to

$$\mu = \frac{\int t \cdot \mathrm{TOF}(t)\mathrm{d}t}{\int \mathrm{TOF}(t)\mathrm{d}t} \qquad (\text{eq 1})$$

where TOF(t) is the time-of-flight signal of the detected peak and μ is the center of gravity of the peak. The contribution of the parent and H-loss ions to the observed peak can now be obtained using

$$\mu = at_1 + (1 - a)t_2 \qquad (\text{eq 2})$$

where t_1 and t_2 are the arrival times of the parent (14.76 μs) and daughter ions (14.70 μs), respectively (Figure 2). The factor a, with $0 \leq a \leq 1$, is the fraction of the parent ions contributing to the observed TOF peak. The resulting breakdown diagrams are shown in Figure 3.

Although the kinetic shift for hydrogen loss is not apparent in the mass spectrum as an asymmetric peak, the shape of the
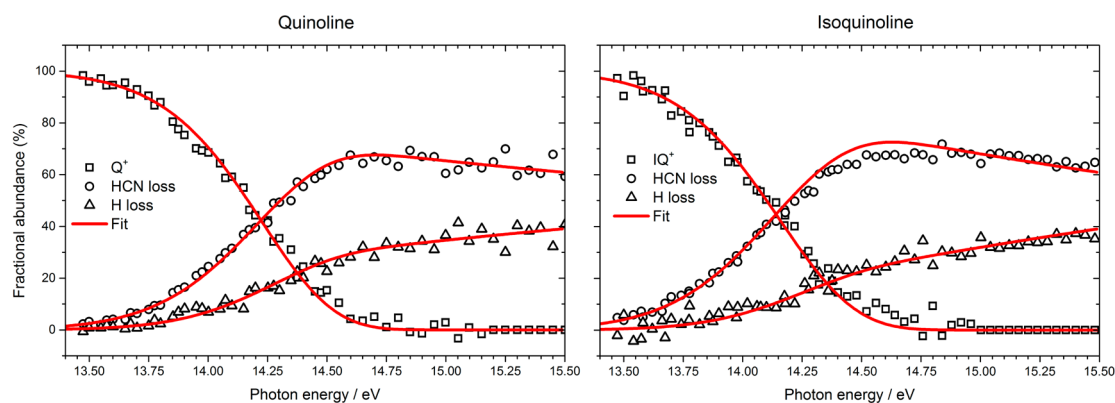
Figure 3. Quinoline (left) and isoquinoline (right) breakdown diagrams (open symbols) plotted together with model fits to the data (solid red lines).

HCN-loss peak (Figure 2) is characteristic of the decay rate of their common parent ion. Hence, the HCN-loss peak yields the sum of the rate constants, and the breakdown diagram yields the branching ratios to apportion this sum to the individual channels. Thus, not only can we determine fractional abundance of the H-loss channel despite its unresolved TOF peak, but also it is possible to derive experimental dissociation rates as a function of photon energy.

4.3. Potential Energy Surfaces. Quantum chemical computations have been performed to shed light on the energetics and structures of the unimolecular dissociation products. In constrained optimizations, bond lengths were scanned while the other internal coordinates were relaxed using the B3LYP/6-311++G(d,p) level of theory. Next, accurate single point energies and frequencies of products, intermediates and transition states were computed using the CBS-QB3 composite method, which also relies on B3LYP geometry optimization to locate minima and saddle points on the potential energy surface but uses extrapolated wave function theory methods to obtain the electronic energies. The main overall pathways for the dissociative ionization are summarized in Scheme 2.

4.3.1. Hydrogen Atom Loss Channel. Hydrogen loss (Scheme 2) can proceed via elimination of either one of the seven hydrogens of the parent C_9H_7N cation (numbering indicated in Scheme 1). The energies required for hydrogen abstraction from the quinoline and isoquinoline cation with respect to the neutral species are listed in Table 1. The computed binding energy of hydrogen atoms is much lower than the photon energy at which the H-loss fragment shows up
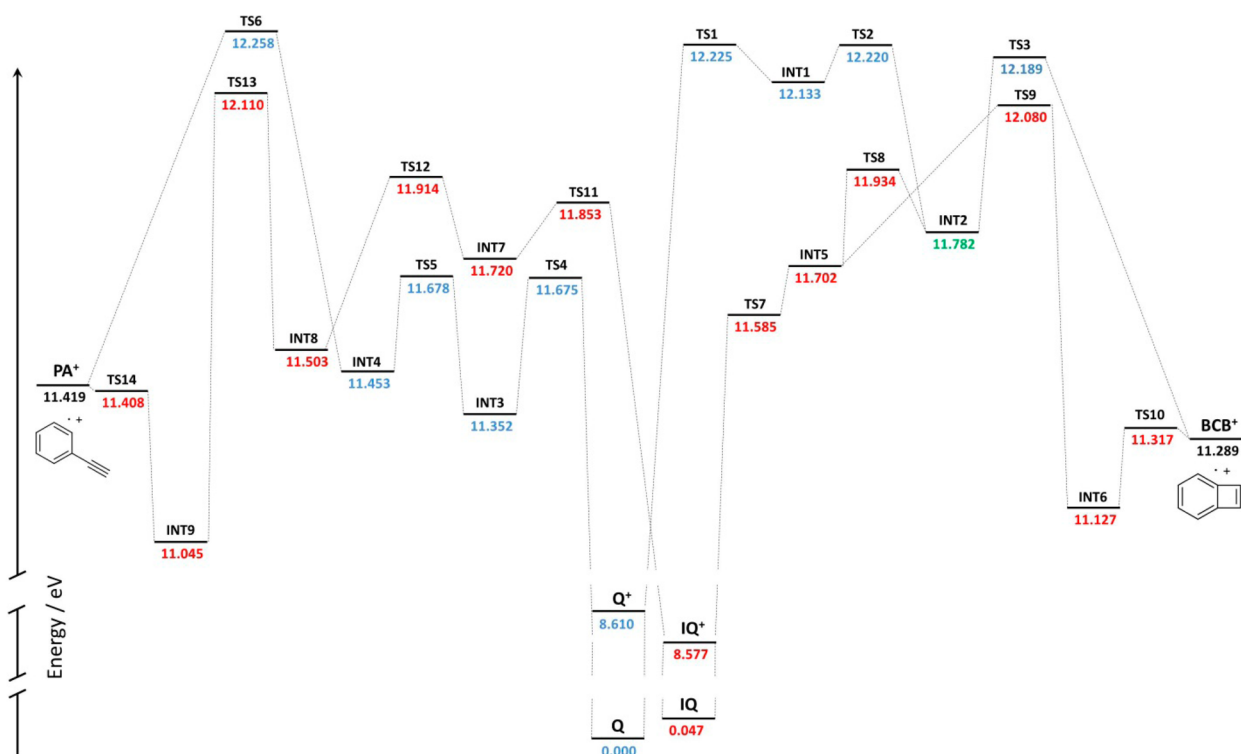
in the breakdown diagram. This confirms the kinetic shift in the hydrogen-loss channel.

The results in Table 1 show that removal of a hydrogen atom from the non-nitrogen-substituted ring requires significantly more energy than removing a hydrogen atom from the N-heterocycle. This contrasts with C−H bond dissociation energies for the unsubstituted PAHs naphthalene[24] and pyrene[42] in which H atoms are nearly equivalent. Removal of an H atom from the "H2" position (Scheme 1) in quinoline and the "H1" position in isoquinoline is energetically most favorable and requires 1 eV (or ∼100 kJ mol^{-1}) less than H removal from the unsubstituted ring. Thus, in contrast with unsubstituted PAHs, H atoms are not expected to lose their positional identity at moderately high energies.

It should be noted that the parent ion has to pass through a conical intersection along the reaction coordinate of the H-loss reaction. The ground state of the parent ion is of A″ symmetry (HOMO in Figure 1), and both the departing $1s^1$ H atom and the closed-shell fragment ion are totally symmetric. Therefore, the fragments only correlate with an (iso)quinoline cation excited electronic state of A′ symmetry. First, calculations have shown that the A″ and A′ reaction energy curves are quasi-degenerate and internal conversion is possible at numerous geometries along the reaction coordinate. Second, even in the naphthalene cation, which exhibits a much larger A″−A′ splitting because of the stabilization of the molecular orbital analogous to the N lone pair type HOMO−2 in (iso)quinoline, H-loss dynamics remained unaffected by the internal conversion dynamics.[24] Thus, it appears to be reasonable to assume that H loss is governed by nuclear dynamics and internal conversion is instantaneous on the time scale of C−H bond breaking.

4.3.2. HCN-Loss Channel. The dominant dissociation channel for both quinoline and isoquinoline is the loss of HCN (Figure 3), which accounts for about 50% of the fragments at 15.5 eV. The daughter ion formed via this channel can exist in either of the two $C_8H_6^{\bullet+}$ isomers, benzocyclobutadiene (BCB), and phenylacetylene (PA), shown in Scheme 2. The paths leading to the formation of these isomers through dissociative ionization have been investigated by quantum chemical computations, summarized in Figure 4. The energies of all structures are referenced to the energy of ground state neutral quinoline. The structures of the transition states (TS) and intermediates (INT) are shown in Figure 5.

4.3.2.1. Formation of $BCB^{\bullet+}$. The lowest energy path to the formation of $BCB^{\bullet+}$ from quinoline is found to proceed via **TS1**

Table 1. CBS-QB3 H-Loss Dissociative Photoionization Thresholds for C−H Bond Breaking in Quinoline and Isoquinoline[a]

Q	E_0/eV	IQ	E_0/eV
H2	11.914	H1	11.903
H3	12.819	H3	12.126
H4	12.888	H4	12.728
H5	12.870	H5	13.209
H6	13.099	H6	13.209
H7	13.024	H7	13.164
H8	13.115	H8	13.208

[a]Refer to Scheme 1 for the labeling of the hydrogen atoms.

Figure 4. Potential energy surface of the dissociative ionization of quinoline (blue) and isoquinoline (red). Note: Only the lowest energy paths are shown.
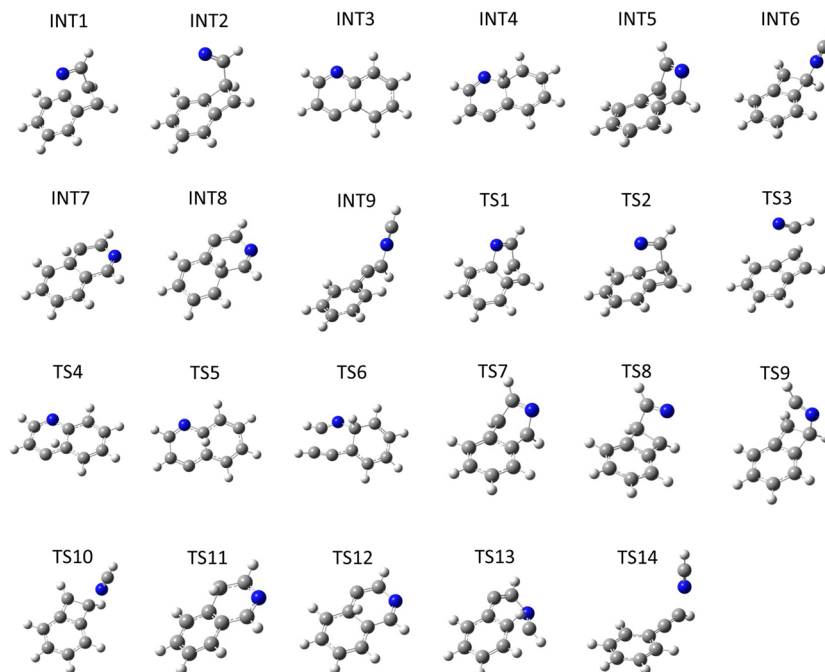
Figure 5. Structures of the intermediates (INT) and transition states (TS) that make up the $C_9H_7N^{\bullet+}$ potential energy surface shown in Figure 4.

at 12.225 eV with respect to the neutral, leading to an intermediate state **INT1** at 12.133 eV. From there, a second intermediate (**INT2**) at 11.782 eV can be formed via **TS2** (12.220 eV), after which BCB$^{\bullet+}$ can be formed via **TS3** at 12.189 eV. The lowest energy path to BCB$^{\bullet+}$ from isoquinoline proceeds via **TS7** (11.585 eV) to form **INT5** (11.702 eV). The computed CBS-QB3 energy for **INT5** is higher than that for **TS7**, although from the imaginary frequency of the vibration it

is confirmed that **TS7** is the correct transition state structure leading to **INT5**. CBS-QB3 uses extrapolated wave function theory to obtain the electronic energy at a molecular geometry determined by density functional theory. This can lead to transition state calculations yielding a lower energy than one of the connected minima. Such discrepancies indicate the inaccuracy of the method for the reaction path calculations, while at the same time providing a reliable estimate of the

potential energy range sampled by the reaction coordinate. Two different intermediates can form from **INT5**, namely **INT2** (11.782 eV) and **INT6** (11.127 eV) via **TS8** (11.934 eV) and **TS9** (12.080), respectively. Next, the formation of BCB$^{\bullet+}$ from **INT2** can proceed via **TS3** (12.189 eV) or from **INT6** via **TS10** (11.317 eV). Note that the potential energy surfaces of quinoline and isoquinoline are connected through **INT2**.

The transition state from the naphthalene cation to BCB$^{\bullet+}$ that corresponds to **TS3** has been calculated at 13.142 eV with the reaction energy of 12.836 eV. The computed reverse barrier is thus on the order of 0.9 eV in the dissociative photoionization of (iso)quinoline by HCN loss as opposed to only 0.3 eV in C_2H_2 loss from the naphthalene cation.

4.3.2.2. Formation of PA$^{\bullet+}$. The formation of PA$^{\bullet+}$ + HCN from quinoline can proceed via a hydrogen shift over **TS4** located at 11.675 eV, forming **INT3** at 11.352 eV followed by a second hydrogen shift over **TS5** (11.678 eV), forming **INT4** at 11.453 eV. PA$^{\bullet+}$ + HCN can be formed from **INT4** by a cleavage of a C–C bond via **TS6** located at 12.258 eV. The path to the formation of PA$^{\bullet+}$ from isoquinoline involves a hydrogen shift via **TS11** at 11.853 eV. The thereby formed intermediate **INT7** (11.720 eV) can undergo a second H-shift over **TS12** (11.914 eV) to form **INT8** (11.503 eV). Ring opening from **INT8** is energetically accessible, forming **INT9** (11.045 eV) via **TS13** at 12.110 eV. PA is formed from **INT9** via **TS14** at 11.408 eV. The computed transition state energy is slightly lower than that of the products but lies within the accuracy of the CBS-QB3 energy computations.

4.3.3. C_2H_2-Loss Contributions. We can only resolve the C_2H_2-loss daughter ion peak ($C_7H_5N^{\bullet+}$ at m/z = 103) at high energies, when both m/z = 102 and 103 are symmetric. Thus, instead of analyzing the C_2H_2-loss signal independently, we can only determine its effect on the uncertainty on the derived HCN-loss appearance energies experimentally. Quantum chemical computations on the $C_7H_5N^{\bullet+}$ product energetics show that the C_2H_2-loss path is more endoergic than HCN loss by more than 1 eV in quinoline and by 0.3 eV in isoquinoline and involves two hydrogen shifts in the latter case. Corresponding to its abundance at high energies in both samples, we assumed a constant, 20% C_2H_2-loss contribution across the breakdown diagram. This made the fit significantly worse but without significantly affecting the derived appearance energies. On the basis of the experimental data and the computed C_2H_2-loss paths, which are more endoergic albeit with potentially looser transition states, the C_2H_2-loss contribution is assumed to appear at higher energies than the HCN-loss signal and remains a minor channel throughout, leaving the uncertainty of the derived HCN-loss appearance energy unaffected, which is determined predominantly by the large kinetic shift and the resulting extrapolation.

4.4. Modeling. The breakdown diagrams shown in Figure 3 are modeled in terms of energy distributions and RRKM rates.[30] Harmonic vibrational frequencies of the neutral parent, the parent cation, and the rate limiting transition states were computed as discussed in the previous section and are used as input together with the computed barrier heights to the formation of the fragment species in the model.

For modeling the experimental data, we take into account the two lowest energy paths leading to the observed products. In the case of quinoline these are the paths leading to BCB$^{\bullet+}$ with **TS1** at 12.225 eV and the lowest barrier leading to H atom loss at 11.914 eV. For isoquinoline, the lowest barrier to the formation of $C_8H_6^{\bullet+}$ is over **TS9** at 12.033 eV (with respect to

the isoquinoline neutral) and leads to BCB$^{\bullet+}$. The lowest barrier to H loss is 11.903 eV. There is no energy maximum along the H-loss coordinate, but the system has to pass a conical intersection. Transition state frequencies for H-loss channels that are used in the model are estimated by optimizing the structure and computing the frequencies with the least bound H atom in the A′ state of the cation at an arbitrarily chosen C–H distance of 3 Å.

The PEPICO program[30] employs RRKM theory to fit the breakdown diagram simultaneously with the time-of-flight distributions to account for kinetic shifts. The fits to the measured data are displayed in Figures 2 and 3. Appearance energies are retrieved from the model fit and are 12.0 ± 0.1 and 11.9 ± 0.1 eV (quinoline), and 12.1 ± 0.2 and 11.6 ± 0.2 eV (isoquinoline) for H loss and HCN loss, respectively. If the dissociation were fast, the 0 K appearance energy would correspond to the disappearance energy of the parent ion in the breakdown diagram.[43] The kinetic shift in the iPEPICO experiment at a 120 V cm^{-1} extraction field, i.e., the excess energy required to lift the dissociation rates above 10^6 s^{-1}, can thus be calculated to be 2.7–3 eV for HCN loss from (iso)quinoline, cf. 4.2 eV for C_2H_2 loss from naphthalene.[24] Furthermore, the error bar on the isoquinoline data is larger than that on the quinoline data. This is caused by a possibly larger contribution of a C_2H_2-loss channel that could lead to somewhat slower apparent dissociation rates.

The experimentally determined energies required for removing a hydrogen atom are ~0.1 eV higher than would be expected on the basis of the quantum chemical computations presented in the previous section (11.914 and 11.903 eV for quinoline and isoquinoline, respectively). The fact that this difference lies within the error bars is somewhat surprising, because RRKM has been shown to overestimate the kinetic shift of dissociations that take place along a purely attractive potential energy curve.[44] However, the system has to pass through a conical intersection, which means that both the reactant and the transition state phase spaces are poorly constrained. The fact that the derived appearance energy is apparently accurate to within 0.1 eV despite the ~3 eV kinetic shift indicates that the extrapolation based on the branching ratios and the statistical model is a quite robust approach to determine the appearance energies.

5. DISCUSSION AND CONCLUSIONS

We have investigated the ionization and dissociative ionization of quinoline and isoquinoline applying the iPEPICO technique and VUV synchrotron radiation. Both isomers exhibit structured $\tilde{X}^+$ and $\tilde{C}^+$ ion state bands in the photoelectron spectrum, which were successfully simulated by calculating Franck–Condon factors, yielding adiabatic ionization energies as well as the active vibrational modes.

The lowest energy dissociative photoionization channels of quinoline and isoquinoline are shown to take place via the loss of a hydrogen atom or an HCN fragment, forming $C_9H_6N^+$, and $C_8H_6^{\bullet+}$, respectively. Reaction paths leading to products are computed, and the measured breakdown curves and time-of-flight distributions are fitted to determine the experimental dissociative photoionization appearance energies. Appearance energies derived from the RRKM model are 11.9 ± 0.1 eV (HCN loss), 12.0 ± 0.1 eV (H loss), and 11.6 ± 0.2 eV (HCN loss), 12.1 ± 0.2 eV (H loss) for the dissociative ionization of quinoline and isoquinoline, respectively.

The results can be compared to a previous study on the dissociative ionization of naphthalene. For photon energies below 18 eV, the dominant channels for naphthalene photodissociation were found to be H loss and C_2H_2 loss, approximately having equal contributions. The loss of C_4H_2 and the loss of two hydrogen atoms were found to be minor, but detectable channels. The presence of the nitrogen atom in quinoline and isoquinoline causes the barrier to dissociation to be significantly reduced. This can be rationalized by the possibility that the nitrogen lone pair participates in a dative bond in the transition state, in which the N atom carries formally the positive charge, which leads to a resonance stabilized TS and a lower lying rate-limiting transition state. The activation energy for HCN removal is 0.90 eV (quinoline) and 1.03 eV (isoquinoline) lower than that for the removal of the isoelectronic C_2H_2 from naphthalene.

Hydrogen loss is observed with a significant kinetic shift at photon energies in excess of the computed barrier. This is probably a consequence of the depth of the potential energy well, i.e., of the stability of the parent cation, together with its relatively large size and not related to the need for A″ → A′ internal conversion along the C−H bond breaking reaction coordinate. Computations indicate that the lowest-energy path to the formation of $C_8H_6^{\bullet+}$ yields $BCB^{\bullet+}$ for both dissociative ionization of quinoline and isoquinoline, and $BCB^{\bullet+}$ is likely the dominant fragment ion at threshold. However, as the activation energy differences are smaller than the uncertainty of the CBS-QB3 method, it is not possible to determine the identity of the fragment ion unambiguously.

Notwithstanding the large kinetic shifts observed in this study, neutral nitrogen heterocyclic species are less photostable than their carbon-only counterparts and this has important implications for their possible presence in the ISM and Titan's upper atmosphere. Extrapolating the findings to larger PAHs that are believed to be responsible for the interstellar mid-IR emission bands, PANHs are less likely to survive in the harsh environments in space than their PAH counterparts, because the nitrogen-containing unit will be readily expelled from the molecule. The photolysis of PANHs in photon dominated regions (PDRs) can possibly serve as a source of HCN. Similar arguments apply to the upper atmosphere of Titan, where energetic photons initiate the ion-neutral chemistry by dissociative ionization.

The reaction of the benzene radical cation with C_2H_2 was studied experimentally by Bohme et al.[45] From their measurements they found that, although some reactions paths are exothermic, the reaction does not yield products or electrostatically bound adducts at room temperature. More recently, this conclusion was supported by Momoh et al.[46] who investigated the reaction of the benzene cation in clusters of acetylene in using the mass-selected ion-mobility drift cell technique. As shown by Soliman et al.,[47] the barrier to addition of C_2H_2 to the benzene radical cation can be eliminated by removal of a hydrogen atom from the cation. The subsequent reaction of the phenylium ion with two C_2H_2 molecules yields $C_{10}H_9^+$, which is likely to be protonated naphthalene. In a different study, Soliman et al.[48] found that the reaction of the pyridinium ion is more favorable and that the presence of a nitrogen atom in the molecule enhances the growth mechanism by sequential C_2H_2 addition. Hence, even though they are less photostable, nitrogen-containing PAHs may still be important species in the upper atmosphere of Titan. Furthermore, the

$C_6H_6^{\bullet+}$ + HCN reaction, followed by a C_2H_2 addition could also be a source of (iso)quinoline in this environment.

The potential energy surfaces presented here also give insight into possible formation paths of quinoline and isoquinoline from $C_8H_6^{\bullet+}$ in the upper atmosphere of Titan. Rate limiting barriers of 0.84 and 0.69 eV are encountered to the formation of quinoline and isoquinoline, respectively, from the reaction between $PA^{\bullet+}$ and HCN. Rate limiting barriers of 0.94 and 0.79 eV are found for the formation of quinoline and isoquinoline, respectively, from $BCB^{\bullet+}$ and HCN. The formation of isoquinoline is thus energetically favored over the formation of quinoline. However, the entrance barriers are rather large, suggesting that alternative reaction paths are more likely formation routes to PANHs.

Finally, the reverse, HCN vs C_2H_2 association reaction to $C_8H_6^{\bullet+}$ to form (iso)quinoline vs naphthalene can be compared on the basis of the reverse barriers and the kinetic shifts observed in dissociative photoionization. The significantly lower reverse barrier for dissociation in C_2H_2 loss in naphthalene cation (0.3 eV) than for HCN loss in the (iso)quinoline cation (0.9 eV) translates into a smaller barrier for the association reaction with C_2H_2. Recent experiments on the $PA^{\bullet+}$ + HCN and $PA^{\bullet+}$ + C_2H_2 association reactions confirm this difference. At room temperature, the C_2H_2 + $PA^{\bullet+}$ reaction was found to yield a covalently bonded $C_{10}H_8^+$ product,[49] whereas the HCN + $PA^{\bullet+}$ reaction was found to yield ion dipole association complexes only.[50] Furthermore, the larger kinetic shift in the naphthalene cation (more than 4 eV, compared with about 3 eV in (iso)quinoline) indicates that, once the activated complex is formed, the reverse dissociation reaction is more likely to be outcompeted by IR fluorescence and collisional cooling in naphthalene than in (iso)quinoline. Thus, even at comparable HCN and C_2H_2 concentrations, $C_8H_6^{\bullet+}$ ions seem to be more likely to form naphthalene than to incorporate a nitrogen atom into the ring. In short, as evidenced by the low abundance of C_2H_2-loss products in the mass spectra, dissociative photoionization will preferably remove nitrogen from PANHs and association reactions are less likely to incorporate nitrogen atoms into the carbon scaffold, indicating the N-inclusion probably takes place at the earliest stages of condensation.

■ **AUTHOR INFORMATION**

Corresponding Author
*J. Bouwman. E-mail: mail:j.bouwman@science.ru.nl.
Notes
The authors declare no competing financial interest.

■ REFERENCES

(1) Weilmünster, P.; Keller, A.; Homann, K. H. Large Molecules, Radicals, Ions, and Small Soot Particles in Fuel-Rich Hydrocarbon Flames: Part I: Positive Ions of Polycyclic Aromatic Hydrocarbons (PAH) in Low-Pressure Premixed Flames of Acetylene and Oxygen. *Combust. Flame* **1999**, *116*, 62−83.

(2) Kozin, I. S.; Larsen, O. F. A.; deVoogt, P.; Gooijer, C.; Velthorst, N. H. Isomer-Specific Detection of Azaarenes in Environmental Samples by Shpol'skii Luminescence Spectroscopy. *Anal. Chim. Acta* **1997**, *354*, 181−187.

(3) Chen, H. Y.; Preston, M. R. Azaarenes in the Aerosol of an Urban Atmosphere. *Environ. Sci. Technol.* **1998**, *32*, 577−583.

(4) Bleeker, E. A. J.; Wiegman, S.; de Voogt, P.; Kraak, M.; Leslie, H. A.; de Haas, E.; Admiraal, W. In *Reviews of Environmental Contamination and Toxicology*; Ware, G. W., Ed.; Springer: Berlin, 2002; Vol. *173*, pp 39−83.

(5) Leger, A.; Puget, J. L. Identification of the Unidentified IR Emission Features of Interstellar Dust. *Astron. Astrophys.* **1984**, *137*, L5−L8.

(6) Allamandola, L. J.; Tielens, A.; Barker, J. R. Polycyclic Aromatic-Hydrocarbons and the Unidentified Infrared-Emission Bands - Auto Exhaust Along the Milky-Way. *Astroph. J.* **1985**, *290*, L25−L28.

(7) Allamandola, L. J.; Tielens, A.; Barker, J. R. Interstellar Polycyclic Aromatic-Hydrocarbons - the Infrared-Emission Bands, the Excitation Emission Mechanism, and the Astrophysical Implications. *Astrophys. J. Suppl. Ser.* **1989**, *71*, 733−775.

(8) Tielens, A. *Annu. Rev. Astron. Astrophys.* **2008**, *46*, 289−337.

(9) Frenklach, M.; Feigelson, E. D. Formation of Polycyclic Aromatic-Hydrocarbons in Circumstellar Envelopes. *Astrophys. J.* **1989**, *341*, 372−384.

(10) Cherchneff, I.; Barker, J. R.; Tielens, A. Polycyclic Aromatic Hydrocarbon Formation in Carbon-Rich Stellar Envelopes. *Astrophys. J.* **1992**, *401*, 269−287.

(11) Mattioda, A. L.; Hudgins, D. M.; Bauschlicher, C. W.; Rosi, M.; Allamandola, L. J. Infrared Spectroscopy of Matrix-Isolated Polycyclic Aromatic Compounds and Their Ions. 6. Polycyclic Aromatic Nitrogen Heterocycles. *J. Phys. Chem. A* **2003**, *107*, 1486−1498.

(12) Douglas, M. H.; Bauschlicher, C. W., Jr.; Allamandola, L. J. Variations in the Peak Position of the 6.2 μm Interstellar Emission Feature: A Tracer of N in the Interstellar Polycyclic Aromatic Hydrocarbon Population. *Astrophys. J.* **2005**, *632*, 316.

(13) Tielens, A. G. G. M. The Molecular Universe. *Rev. Mod. Phys.* **2013**, *85*, 1021−1081.

(14) Coates, A. J.; Crary, F. J.; Lewis, G. R.; Young, D. T.; Waite, J. H.; Sittler, E. C. Discovery of Heavy Negative Ions in Titan's Ionosphere. *Geophys. Res. Lett.* **2007**, *34*, L22103.

(15) Waite, J. H.; Young, D. T.; Cravens, T. E.; Coates, A. J.; Crary, F. J.; Magee, B.; Westlake, J. The Process of Tholin Formation in Titan's Upper Atmosphere. *Science* **2007**, *316*, 870−875.

(16) Wilson, E. H.; Atreya, S. K. Chemical Sources of Haze Formation in Titan's Atmosphere. *Planet. Space Sci.* **2003**, *51*, 1017−1033.

(17) Lavvas, P.; Sander, M.; Kraft, M.; Imanaka, H. Surface Chemistry and Particle Shape: Processes for the Evolution of Aerosols in Titan's Atmosphere. *Astroph. J.* **2011**, *728*, 11.

(18) Vuitton, V.; Yelle, R. V.; McEwan, M. J. Ion Chemistry and N-Containing Molecules in Titan's Upper Atmosphere. *Icarus* **2007**, *191*, 722−742.

(19) Imanaka, H.; Smith, M. A. Formation of Nitrogenated Organic Aerosols in the Titan Upper Atmosphere. *Proc. Natl. Acad. Sci. U. S. A.* **2010**, *107*, 12423−12428.

(20) Krasnopolsky, V. A. A Photochemical Model of Titan's Atmosphere and Ionosphere. *Icarus* **2009**, *201*, 226−256.

(21) Imanaka, H.; Khare, B. N.; Elsila, J. E.; Bakes, E. L. O.; McKay, C. P.; Cruikshank, D. P.; Sugita, S.; Matsui, T.; Zare, R. N. Laboratory Experiments of Titan Tholin Formed in Cold Plasma at Various Pressures: Implications for Nitrogen-Containing Polycyclic Aromatic Compounds in Titan Haze. *Icarus* **2004**, *168*, 344−366.

(22) Ricca, A.; Bauschlicher, C. W., Jr; Bakes, E. L. O. A Computational Study of the Mechanisms for the Incorporation of a Nitrogen Atom into Polycyclic Aromatic Hydrocarbons in the Titan Haze. *Icarus* **2001**, *154*, 516−521.

(23) Landera, A.; Mebel, A. M. Mechanisms of Formation of Nitrogen-Containing Polycyclic Aromatic Compounds in Low-Temperature Environments of Planetary Atmospheres: A Theoretical Study. *Faraday Discuss.* **2010**, *147*, 479−494.

(24) West, B.; Joblin, C.; Blanchet, V.; Bodi, A.; Sztaray, B.; Mayer, P. M. On the Dissociation of the Naphthalene Radical Cation: New iPEPICO and Tandem Mass Spectrometry Results. *J. Phys. Chem. A* **2012**, *116*, 10999−11007.

(25) Hemberger, P.; Bodi, A.; Gerber, T.; Wuertemberger, M. Radius, U. Unimolecular Reaction Mechanism of an Imidazolin-2-Ylidene: An Ipepico Study on the Complex Dissociation of an Arduengo-Type Carbene. *Chem.—Eur. J.* **2013**, *19*, 7090−7099.

(26) Baer, T.; Walker, S. H.; Shuman, N. S.; Bodi, A. One- and Two-Dimensional Translational Energy Distributions in the Iodine-Loss Dissociation of 1,2-$C_2H_4I_2^+$ and 1,3-$C_3H_6I_2^+$: What Does This Mean? *J. Phys. Chem. A* **2012**, *116*, 2833−2844.

(27) Rowland, T. G.; Borkar, S.; Bodi, A.; Sztáray, B. Iodine Atom Loss Kinetics in Internal Energy Selected 1-Iodoalkane Cations by Imaging Photoelectron Photoion Coincidence Spectroscopy. *Int. J. Mass Spectrom.* **2015**, DOI: 10.1016/j.ijms.2014.07.028.

(28) Bodi, A.; Johnson, M.; Gerber, T.; Gengeliczki, Z.; Sztaray, B.; Baer, T. Imaging Photoelectron Photoion Coincidence Spectroscopy with Velocity Focusing Electron Optics *Rev. Sci. Instrum.* **2009**, *80*.

(29) Johnson, M.; Bodi, A.; Schulz, L.; Gerber, T. Vacuum Ultraviolet Beamline at the Swiss Light Source for Chemical Dynamics Studies. *Nucl. Instrum. Methods A* **2009**, *610*, 597−603.

(30) Sztaray, B.; Bodi, A.; Baer, T. Modeling Unimolecular Reactions in Photoelectron Photoion Coincidence Experiments. *J. Mass Spectrom.* **2010**, *45*, 1233−1245.

(31) Sztaray, B.; Baer, T. Suppression of Hot Electrons in Threshold Photoelectron Photoion Coincidence Spectroscopy Using Velocity Focusing Optics. *Rev. Sci. Instrum.* **2003**, *74*, 3763−3768.

(32) Bodi, A.; Hemberger, P. Imaging Breakdown Diagrams for Bromobutyne Isomers with Photoelectron-Photoion Coincidence. *Phys. Chem. Chem. Phys.* **2014**, *16*, 505−515.

(33) Frisch, M. J.; Trucks, G. W.; Schlegel, H. B.; Scuseria, G. E.; Robb, M. A.; Cheeseman, J. R.; Scalmani, G.; Barone, V.; Mennucci, B.; Petersson, G. A.; et al. *Gaussian 09*, Revision D.01; Gaussian, Inc.: Wallingford, CT, 2009.

(34) Montgomery, J. A.; Frisch, M. J.; Ochterski, J. W.; Petersson, G. A. A Complete Basis Set Model Chemistry. VI. Use of Density Functional Geometries and Frequencies. *J. Chem. Phys.* **1999**, *110*, 2822−2827.

(35) Montgomery, J. A.; Frisch, M. J.; Ochterski, J. W.; Petersson, G. A. A Complete Basis Set Model Chemistry. VII. Use of the Minimum Population Localization Method. *J. Chem. Phys.* **2000**, *112*, 6532−6542.

(36) Mozhayskiy, A.; Krylov, A. I. *ezSpectrum*; University of Southern California: Los Angeles, CA; http://iopenshell.usc.edu/downloads/.

(37) Terenin, A. *Proceedings of the Chemical Society*; RSC: London, 1961; pp 321−356.

(38) Brogli, F.; Heilbronner, E.; Kobayashi, T. Photoelectron Spektra of Azabenzenes and Azanaphthalenes: II. A Reinvestigation of Azanaphthalenes by High-Resolution Photoelectron Spectroscopy. *Helv. Chim. Acta* **1972**, *55*, 274−288.

(39) Schäfer, W.; Schweig, A.; Vermeer, H.; Bickelhaupt, F.; De Graaf, H. On the Nature of the "Free Electron Pair" on Phosphorus in Aromatic Phosphorus Compounds: The Photoelectron Spectrum of 2-Phosphanaphthalene. *J. Electron Spectrosc. Relat. Phenom.* **1975**, *6*, 91−98.

(40) Mayer, P. M.; Blanchet, V.; Joblin, C. Threshold Photoelectron Study of Naphthalene, Anthracene, Pyrene, 1,2-Dihydronaphthalene, and 9,10-Dihydroanthracene *J. Chem. Phys.* **2011**, *134*.

(41) Shao, Y.; Molnar, L. F.; Jung, Y.; Kussmann, J.; Ochsenfeld, C.; Brown, S. T.; Gilbert, A. T. B.; Slipchenko, L. V.; Levchenko, S. V.;

O'Neill, D. P.; et al. Advances in Methods and Algorithms in a Modern Quantum Chemistry Program Package. *Phys. Chem. Chem. Phys.* **2006**, *8*, 3172−3191.

(42) West, B.; Useli-Bacchitta, F.; Sabbah, H.; Blanchet, V.; Bodi, A.; Mayer, P. M.; Joblin, C. Photodissociation of Pyrene Cations: Structure and Energetics from $C_{16}H_{10}^+$ to C_{14}^+ and Almost Everything in Between. *J. Phys. Chem. A* **2014**, *118*, 7824−7831.

(43) Bodi, A.; Csontos, J.; Kallay, M.; Borkar, S.; Sztaray, B. On the Protonation of Water. *Chem. Sci.* **2014**, *5*, 3057−3063.

(44) Stevens, W.; Sztaray, B.; Shuman, N.; Baer, T.; Troe, J. Specific Rate Constants k(E) of the Dissociation of the Halobenzene Ions: Analysis by Statistical Unimolecular Rate Theories. *J. Phys. Chem. A* **2009**, *113*, 573−582.

(45) Bohme, D. K.; Wlodek, S.; Zimmerman, J. A.; Eyler, J. R. Formation of $C_{10}H_8^+$ from the Benzene Radical Cation - a Case for the Growth of Polycyclic Aromatic Hydrocarbon Ions by Ion Molecule Reactions in the Gas-Phase. *Int. J. Mass Spectrom. Ion Processes* **1991**, *109*, 31−47.

(46) Momoh, P. O.; Soliman, A.-R.; Meot-Ner, M.; Ricca, A.; El-Shall, M. S. Formation of Complex Organics from Acetylene Catalyzed by Ionized Benzene. *J. Am. Chem. Soc.* **2008**, *130*, 12848−12849.

(47) Soliman, A.-R.; Hamid, A. M.; Momoh, P. O.; El-Shall, M. S.; Taylor, D.; Gallagher, L.; Abrash, S. A. Formation of Complex Organics in the Gas Phase by Sequential Reactions of Acetylene with the Phenylium Ion. *J. Phys. Chem. A* **2012**, *116*, 8925−8933.

(48) Soliman, A.-R.; Hamid, A. M.; Attah, I.; Momoh, P.; El-Shall, M. S. Formation of Nitrogen-Containing Polycyclic Cations by Gas-Phase and Intracluster Reactions of Acetylene with the Pyridinium and Pyrimidinium Ions. *J. Am. Chem. Soc.* **2013**, *135*, 155−166.

(49) Soliman, A.-R.; Attah, I. K.; Hamid, A. M.; El-Shall, M. S. Growth Kinetics and Formation Mechanisms of Complex Organics by Sequential Reactions of Acetylene with Ionized Aromatics. *Int. J. Mass spectrom,* **2015**, DOI: 10.1016/j.ijms.2014.08.023.

(50) Hamid, A. M.; Soliman, A.-R.; Samy El-Shall, M. Assembly of Hcn Hydrogen Bonding Chains in the Gas Phase. Binding Energies and Structures of Phenylacetylene$^+$(HCN)$_n$ Clusters, n=1−4. *Chem. Phys. Lett.* **2012**, *543*, 23−27.